Synergetic Effect in $Ru_xMo_{(1-x)}S_2$/SBA-15 Hydrodesulfurization Catalysts: Comparative Experimental and DFT Studies

T.A. Zepeda[1*], N.L. Torres-García[2], J. Antúnez-García[1], D.H. Galván[1], B. Pawelec[3*], R. Huirache-Acuña[2], J.N. Díaz de León[1], G. Alonso-Núñez[1], J.L.G. Fierro[3] and S. Fuentes[1]

[1] Universidad Nacional Autónoma de México, Centro de Nanociencia y Nanotecnología, Apdo. Postal 14, 22800 Ensenada, B.C. México.
[2] Universidad Michoacana de San Nicolás de Hidalgo, Facultad de Ingeniería Química, Ciudad Universitaria, 58060, Morelia, Michoacán, México.
[3] Instituto de Catálisis y Petroleoquímica, CSIC, Cantoblanco, 28049 Madrid, Spain.

* Corresponding author: bgarcia@icp.csic.es; trino@cnyn.unam.mx

Abstract

The effect of introducing Ru impurities into the MoS_2 crystalline structure of the sulfided $Ru_xMo_{(1-x)}S_2$/SBA-15 catalysts have been investigated using density functional theory (DFT) calculations and the catalyst characterization by different techniques (chemical analysis (ICP-AES), temperature-programmed reduction (TPR), X-ray diffraction (XRD), N_2 physisorption, DRIFTS of adsorbed pyridine (DRIFTS-Py) and X-ray photoelectron spectroscopy (XPS)). The catalyst activity was tested in the hydrodesulfurization (HDS) of dibenzothiophene (DBT) reaction carried out in a batch reactor, T = 320 ºC and total H_2 pressure of 5.5 MPa. From electronic structure DFT calculations is was concluded that the 4d orbitals of both Mo and Ru played an important role in the catalyst optimization being the processes of transport and charge transference the most important ones. It was found that the enrichment with Ru, promotes a greater electronic participation (DOS at the Fermi level) of the different atoms in the $Ru_xMo_{(1-x)}S_2$ phase leading to metallization of the Mo ions. The catalyst activity in HDS of DBT reaction demonstrated a similar behavior to that of theoretical density of states (DOS) calculated *via* DFT. All bimetallic systems presented the synergetic effect between Ru and Mo in the HDS of DBT reaction over $Ru_xMo_{(1-x)}S_2$/SBA-15 catalysts. The highest activity observed for Ru content of x = 0.4 was consistent with theoretical results predicting that the optimum DOS contributions should be around x = 0.44. The most active $Ru_{0.4}Mo_{0.6}S_2$/SBA-15 exhibit the best hydrogenation properties linked with the Ru-induced metallization of Mo ions in the $Ru_{0.4}Mo_{0.6}S_2$ phase. This catalyst showed two-fold higher hydrogenation properties than $CoMoS$/γ-Al_2O_3 reference catalyst. The linear dependencies of initial activity on Brønsted-to-Lewis acidities ratio (from DRIFT-Py) and total metal surface exposure (from XPS) were observed.

1. Introduction.

Although nowadays, there is an increasing tendency to reduce the production of energy through fossil fuels [1-3], the requirements of fuels obtained from crude oil still have a considerable demand. Moreover, the sulfur content in fuels decrease the quality of combustion in the engine and the efficiency of catalytic converters in cars, and consequently, the amount of pollutants emitted towards the environment. Reason why environmental regulations such as the European Standards Organization (CEN), since 2009 a limit of sulfur content of up to 10 ppm was fixed for both gasoline and diesel. Commonly in the petrochemical industry, hydrotreating catalytic processes are used to remove heteroatoms (the sulfur between them) fixed to organic moieties. Catalysts traditionally used for hydrodesulphurisation (HDS) processes consist of supported metal transition sulphides, which are elements corresponding to groups 6 and 8-10 of the periodic table.

Of these, the most common are MoS_2, WS_2 and their compounds formed with Co and Ni (known as CoMo, NiMo and NiW). However, these catalysts demonstrated some limited efficiency required to remove sulfur from the heavy oil fraction [4].

Since the pioneering work by Pecoraro and Chianelli [4], the catalysts based on RuS_2 demonstrated to be one of the most effective catalytic systems for desulfurization processes [5-18]. The high HDS activity of the monometallic RuS_2/Al_2O_3 catalyst was ascribed to easy stabililization of the sulfur species upon reaction conditions employed and high intrinsic hydrogenation activity of Ru [9]. Indeed, the enhancement of the HDS activity and selectivity toward hydrogenation route products was observed after Ru incorporation into a commercial $Ni(Co)Mo/Al_2O_3$ sulfide catalysts [10-14].

The effect of Ru incorporation onto the alumina-supported Mo sulfides was extensively studied [15-20]. However, the data on the synergy in HDS over those systems are contradictory [20]. This is probably because synergy between Ru and Mo depends strongly on the catalyst pretreatment before sulfidation [15] and the catalyst preparation method employed [18]. A high level of HDS synergy observed for the properly prepared the Ru–Mo sulfides was ascribed to formation of the decorated Ru–Mo–S phase rather than formation of ternary sulfide [18]. Unfortunately, it was found that Ru located in the decoration positions on the MoS_2 edges has a low stability and upon reaction conditions tends to segregate pure RuS_2 phase [19-20]. The goal is therefore to enhance the ruthenium-to molybdenum binding energy, allowing a formation of $Ru_xMo_{(1-x)}S_2$ solid solution.

Because a lower ability of RuS_2 and MoS_2 phases to form self-bonds with materials having electronically neural framework, the formation of $Ru_xMo_{(1-x)}S_2$ solid solution should be favored on the silica supports. Among different siliceous materials, one of the most interesting is SBA-15 material showing ordered mesoporous structure. Indeed, it has been

shown that SBA-15 could be suitable carrier for preparing metal sulfide-based HDS catalysts [21 and references within]. The advantages of this material with respect to alumina carrier include its large specific surface area (above 1000 $m^2 \cdot g^{-1}$), uniform-sized pores in the range 4–30 nm, thick framework walls, complementary textural porosity and high thermal stability [22]. In addition, the parallel channel system of SBA-15 might act as a microreactor in which the reactant and the intermediary products might to have prolonged contact with the active phase [23].

Besides the interesting textural properties of mesoporous SBA-15 material, the effect of supporting RuS_2 phase on this substrate in the catalyst activity in HDS reaction was scarcely investigated [21, 24-27]. Romero-Pérez *et al.* [24] observed that RuS_2-pyrite phase supported on SBA-15 and Zr-SBA-15 demonstrated higher activity in the HDS of the DBT than that supported on Al-SBA-15. The catalysts sulfided at 500 °C showed larger activities, because of the formation of a greater quantity of the RuS_2-pyrite structure and a higher dispersion of the active phase [24]. Similarly, the presence of a small amount of cubic RuS_2 phase on the surface of trimetallic Ru_xMoNi/SBA-15 sulfide system enhanced its HDS activity [27].

In line with the above, this work was undertaken with the aim to provide further understanding of the catalytic performance of ternary Ru-Mo-S/SBA-15 sulfide catalysts in deep HDS of DBT reaction. According to Chianelli [28], a fundamental property of the catalysts used for hydrodesulfurization comes from the ability of the 4d and 5d orbitals (of noble metals) to self-bonding, and consequently, from a high covalence degree. Therefore, the primary objective of this work was to study using DFT calculations how the electronic properties of MoS_2 phase change when Ru impurities are introduced. Correlating the experimental and theoretical characterization results with the catalyst performance allows us to determine the relationship between activity and catalyst properties. The properties of Ru-Mo-S/SBA-15 catalytic systems are discussed in terms of the formation of a crystalline solid $Ru_xMo_{(1-x)}S_2$ solid solution. To the best of our knowledge, there are not works describing the effect of formation of crystalline ternary Ru-Mo-S sulfides on the HDS activity.

2. Experimental.

2.1. Density Functional Theory (DFT) Calculations.

For the current work, we started by considering the unit cell for bulk 2H-MoS_2 (space group, P 63/mmc [29]. This initial unit cell was modified by exchanging Mo for Ru atoms, and then to construct the distinct $Ru_xMo_{(1-x)}S_2$ compounds, where x= 0.0, 0.1, 0.2, 0.4, 0.6 and 1.0 (see Figure 1). For completeness, the RuS_2 (space group, $Pm\overline{3}$ [30]) crystalline structure was also included in the present study.

The search of the ground state configurations was performed by using a geometrical optimization through the DFT method, using the DMol^3 program package [31-33]. For this task, the Perdew, Burke and Ernzerhof (PBE) gradient-corrected functional [34], was employed for the exchange correlation energy. The expansion of wave functions of the different atomic species under consideration was studied using the double numerical with a d and p polarization (DNP) basis set (comparable to 6-31G, 6- 31G(d) and 6- 31G(d,p) Gaussian-type basis sets), thus taking into account the electron interactions reasonably. To evaluate the parameters of the present calculations, in Table 1 are compared the lattice constants and band gap values obtained theoretically for bulk MoS_2 and RuS_2 structures versus their experimental counterpart.

Although theoretical/experimental values within for RuS_2 fit very well, for MoS_2 show certain discrepancies, similar to that reported in other theoretical works [35-39]. Although other pseudopotential might have been chosen to make the MoS_2 values more compatible with the experimental ones, however, it was found that doing so would make worse those predicted for RuS_2. Then the parameters employed in the present work were chosen so that not only MoS_2 and RuS_2 compounds but also the distinct $Ru_xMo_{(1-x)}S_2$ phases were reasonably described.

2.2 Support and Catalyst preparation.

The SBA-15 support was synthesized by following a procedure similar to that described by Zhao [40] and Yue [41]. The solid product obtained was filtered, dried at room temperature for 24 h and then at 120 ºC for 3 h, and finally calcined in air at 500 ºC for 6 h with a heating rate of 1 ºC/min. The $Ru_xMo_{(1-x)}S_2$/SBA-15 catalysts in which ruthenium concentration was varied (x = 0.0, 0.1, 0.2, 0.4, 0.6 and 1.0), were prepared by the simultaneous impregnation method using the pore filling method source following the published procedure [42]. The ammonium heptamolybdate (99 % purity, Aldrich) and ruthenium chloride hydrated (99 % purity, Aldrich) were used as molybdenum and ruthenium sources, respectively, and citric acid as chelating agent. Taking into account the difference of the atomic weights between Mo and Ru elements, the samples were prepared with the same total atomic loading of 1.26 mmol per gram of catalysts and an atomic ratio of citric acid/(Mo+Ru) equal to 1.75. The obtained samples were dried at room temperature for 18 h and then at 100 ºC for 2 h. Finally, the samples were calcined at 400 ºC for 4.5 h, reaching this temperature in 3.5 h.

2.3. Characterization of Catalysts.

2.3.1. Chemical Analysis.

The accurate Ru and Mo loadings were quantified using inductively coupled plasma-optical emission spectroscopy on a Perkin Elmer Optima DV 3300 optical emission

spectrometer. Prior to analysis, the samples were digested in a mixture of HF, HCl and HNO_3 in a microwave oven for 2 h, and the calibrations were performed using Ru and Mo standard solutions.

2.3.2. Temperature-Programmed Reduction (H_2-TPR).

TPR experiments of calcined samples were conducted in an ChemBET Pulsar™ TPR/TPD equipment. Prior to reduction, the catalysts (ca. 75 mg) were heated at a rate of 20 ºC.min^{-1} up to a temperature of 150 ºC, and kept for 2 h under a flow of He to remove water and other contaminants. The samples were cooled to ambient temperature in the same He flow; then reduced in flowing gas containing 5% H_2/N_2 at a total flow rate of 100 mL min^{-1}, and finally heated at a rate of 15 ºC min^{-1} up to a final temperature of 900 ºC.

2.3.3. X-Ray Diffraction (XRD).

The X-ray patterns of sulfided catalysts in the 2θ interval of 10–80^0 at a step of 0.028 were recorded on a Philips diffractometer model X'pert, using Cu Kα radiation (λ = 0.1541 nm).

2.3.4. N_2 Adsorption–Desorption Isotherms.

The textural properties of sulfided samples were determined by N_2 adsorption-desorption isotherms recorded at -196 ºC with a TriStar II 3020 Micromeritics equipment. The volume of adsorbed N_2 was normalized to standard temperature and pressure. Specific surface area (S_{BET}) was calculated by applying the BET equation to the range of relative pressures $0.05 < P/P_0 < 0.30$. The average pore diameter was calculated following the Barret-Joyner-Halenda method (BJH) and using the adsorption branch of the N_2 isotherm. The cumulative pore volume was obtained from the isotherms at $P/P_0 = 0.99$.

2.3.5. X-Ray Photoelectron Spectroscopy (XPS).

Photoelectron spectra of the freshly sulfide catalysts were recorded on a A RIBER LDM-32 equipped with a hemispherical electron analyzer and a Mg Kα ($h\nu$ = 1253.6 eV) X-ray source. In order to protect the freshly sulfides catalysts from the air contact, they were kept in argon atmosphere until being transferred into the analysis chamber. The samples were first degassed at 10^{-5} mbar in the pretreatment chamber before being transferred to the analysis chamber, where residual pressure was kept below 7x10^{-9} mbar during data acquisition. The binding energies (BE) were referenced to the C 1s peak (284.5 eV) to account for charging effects. Mixed Gaussian/Lorentzian functions were employed after background subtraction according to Shirley. Surface atomic ratios were computed

from the peak area ratios normalized by the corresponding atomic sensitivity factors provided with manufacturer.

2.3.6. *Diffuse Reflectance Infrared Fourier Transform Spectroscopy of Adsorbed Pyridine (DRIFTS-Py).*

The acidity of sulfide catalysts was evaluated by DRIFT spectroscopy of adsorbed pyridine. Spectra were recorded with an Agilent 660 FTIR spectrophotometer at a resolution of 4 cm^{-1} equipped with a Praying Mantis diffuse reflection attachment and a low temperature cell (Harrick) for *in-situ* measurements. Before analysis, the samples were sulfided *ex-situ* with a 15% H_2S/H_2 mixture at 400 °C for 1 h and then degassed under 10^{-5} mbar for 1 h. The pyridine adsorption was performed at 100 °C and 5 mbar for 30 min. The DRIFT spectra were recorded after evacuation (10^{-5} mbar) of physically adsorbed pyridine at 120 °C for 0.5 h. The Brønsted-to-Lewis acidities ratio (B/L ratio) was estimated using the relative surfaces of the bands at 1541 cm^{-1} (Brønsted) and 1443 cm^{-1} (Lewis) and the molar extinction absorption coefficients of these two bands (B: 1.13 cm ·µmol^{-1}; L: 1.28 cm· µmol^{-1}) reported by Guisnet et al. [43].

2.3. *Catalytic Activity.*

Catalytic activities of the $Ru_xMo_{(1-x)}S_2$/SBA-15 catalysts were evaluated in the HDS of DBT reaction. A laboratory-synthetized CoMo/γ-Al_2O_3 sulfide catalyst was used as reference. The mean physico-chemical properties of this reference catalyst are as follows: 12% wt.% of Mo, 1.8% wt.% of P, Co/(Co + Mo) molar ratio of 0.32, S_{BET}= 228 m^2·g^{-1}, pore diameter of 9.5 nm and total pore volume of 0.55 cm^3·g^{-1}. Before each reaction, the catalysts were activated by *ex-situ* sulfidation using a gas mixture of H_2/H_2S (15 vol. % H_2S) with a flow of 40 mL min^{-1} at and 400 °C for 2 h (5 °C ·min^{-1}). Before catalyst loading, the reactor was purged with an inert gas in order to eliminate residual air. Then, the reactor was loaded with approximately 0.2 g of pre-sulfided catalyst (-80/+100 mesh), 500 ppm of S from DBT and 100 mL of n-hexadecane used as a solvent. The HDS of DBT reaction was carried out in a batch Parr reactor at 320 °C and a hydrogen pressure of 5.5 MPa. A stirring rate of 800 rpm was employed. Reaction products were analyzed by gas chromatography (GC) with an Agilent 7890 gas chromatograph equipped with an Agilent 30 m HP−5 capillary column. The samples were taken every 20 min during the first hour, then every 30 min for the next 4 h. The reduction of feed volume due to sampling was < 5% of total volume. Catalytic activity was expressed in terms of % conversion of DBT versus reaction time. The mean standard deviation for conversion measurements was about 3%. Using conversion data, the initial reaction rate (expressed as mol of DBT converted per second and per gram of catalyst) was calculated for each catalyst.

The reaction products of the HDS of DBT were biphenyl (BP), dicyclohexyl (DCH) and cyclohexylbenzene (CHB). For all catalysts, tetrahydrodibenzothiophene (THDBT) product was not detected by the GC analysis. As seem in Scheme 1, those products are formed through two parallel reaction routes [44]: biphenyl is formed through the direct desulfurization pathways (DDS) whereas cyclohexylbenzene and dicyclohexyl are formed through the hydrogenation pathway (HYD). Thus, the HYD/DDS selectivities ratio was calculated by the equation:

HYD/DDS = [CHB] + [DCH] / [BP]

3. Results and discussion.

3.1. Density Functional Theory (DFT) calculations.

In order to follow the changes in the electronic state of the MoS_2 phase as a function of Ru loading, the DFT calculations were carried out. Band structures for some compounds under study are show in Figure 2. As seen, the separately MoS_2 and RuS_2 compounds (Figures 2 (a) and 2(b)) present a semiconductor character, but when a Ru impurity is introduced into the MoS_2 crystalline structure to form the $Ru_xMo_{(1-x)}S_2$ solid solution (Figures 2 (c) and (d)), a metallic character is developed. This behavior stands at least for the different x values considered here. Due to the electronic properties of a crystalline structure are mainly manifested at the Fermi level, Figure 3 shows the partial density of states (PDOS) and Mulliken charge for S, Mo and Ru atoms as a function of the concentration x. The PDOS for distinct atoms as a function of the Ru concentration x is plotted at this point. In these figures it is observed that for Ru-free MoS_2 compound, the [Mo]3d orbital is the one that participates at the Fermi level, whereas for RuS_2 ($x = 1$) it presents a higher relative participation through [Ru]4d and hybridized [S]3p and [S]3d orbitals. For $x \neq 0$, it is observed that the effect of introducing Ru impurities into the MoS_2 crystalline structure is to increase the density of states available at the Fermi level. Particularly it is observed that while [Mo]3d orbital presents a maximum at $x = 0.25$, both [S]3p and [Ru]4d orbitals present it at $x = 0.44$ which also agrees with that of the maximum total DOS (at the Fermi level) corresponding to this concentration value. This indicates that the metallic character of the molybdenum ions increased when the ruthenium ions are incorporated.

To get more insight about electronic properties of the $Ru_xMo_{(1-x)}S_2$ solid solution, we carried out a population analysis to compute the Mulliken charges. In Figures 3 (d)-3(f) the Mulliken charges values for distinct atomic species are plotted as a function of Ru content x. Results for MoS_2 and RuS_2 composites ($x = 0$ and $x = 1$, respectively), show Mulliken charges values with practically null dispersion. When Ru impurities are introduced into the MoS_2 crystalline structure ($x \neq 0$ or $x \neq 1$), a dispersion on charge is observed mainly for S atoms (Figure 3 (d)). In addition, Figures 3 (d)-(f) show that for some x values, distinct

atoms present both positive and negative charge polarities, thus displaying an amphoteric behavior. Interesting is that the only solid solution for which all the distinct atoms present amphoteric behavior simultaneously corresponds to $x = 0.44$. Thus the reason why the highest contribution to the total density of states (Figures 3(a)-(c)) is at $x = 0.44$, is because an atom not only can donate or accept electrons with atoms of different species, but also with those of the same nature. It should be noted that we just mapped some particular compositional values of x. However, the results suggest that it is possible to find an even better solid solution and this must be found around $x = 0.44$. For this concentration value ($x = 0.44$), the total density of states is maximum due to: (a) the charge polarity distribution around 0 is symmetric (tuned) for all atoms, and (b) the charge magnitude for all the atoms is the same or almost the same. Under these conditions, an electron could jump from one atom to another without distinguishing the species, as in a medium with negligible resistance (ballistic conduction). In conclusion, one can assume that the incorporation of ruthenium ions could promote a synergistic effect between Mo and Ru ions, resulting in an increase of the metallic character of the molybdenum ions, observing the highest effect on the metallicity around $x = 0.44$ value.

Since 2H-MoS$_2$ crystallizes into a trigonal-prismatic coordination for the metal, the effect of the trigonal-prismatic crystal field (CEF) is to lift the five-fold degeneracy of the d-orbitals providing three distinct energy values in the crystal [45-46]. Two of these values are doubly degenerate and one of them is single degenerate. These values are: (a) d_{z2}, (b) d_{x2-y2}, d_{xy}, (c) d_{yz} and d_{xz}. There is a big body of discussion about their ordering, but all the works agree that d_{z2} is the lowest in energy. Our results for 2H-MoS$_2$ agree with the expected analysis. Moreover, Mo d-orbitals interact with S p-orbitals of the same symmetry, forming a hybridized interaction for this compound (2H-MoS$_2$). In order to form the new Ru$_{(x)}$Mo$_{(1-x)}$S$_2$ structure, Ru was introduced into it with different percentage until the desired structure was obtained keeping the original 2H-MoS$_2$ (trigonal-prismatic) configuration throughout the analysis. Henceforth, Ru s-orbitals contribute with the hybridized orbital produced by MoS$_2$ for a final d-p-s orbital interaction, consequently a metallization of the molybdenum ions occurred.

3.2. Characterizations of the Oxide Catalysts.

The chemical characteristics of Ru$_x$Mo$_{(1-x)}$/SBA-15 oxide catalysts are shown in Table 2. As seen in this table, the Ru and Mo content determined by ICP-AES analysis is close to the nominal one. This is because, taking into account the volatility of ruthenium oxide species [47], careful calcination was employed in order to avoid as much as possible ruthenium phases loses. The amount of ruthenium increases with decreasing molybdenum content being the atomic Ru/(Ru + Mo) ratio obtained by chemical analysis close to the nominal one.

Temperature programmed reduction technique (TPR-H_2) was employed to check the effect of Ru incorporation on the reducibility of supported MoO_3 species. The TPR profiles of calcined $Ru_xMo_{(1-x)}$/SBA-15 catalysts are shown in Figure 4. The TPR profile of monometallic Ru/SBA-15 catalyst exhibits a unique H_2 consumption peak at 220 ºC (Figure 4(e)), which corresponds to reduction of RuO_2 to metallic Ru ($RuO_2 + 2H_2 \rightarrow Ru + 2 H_2O$) [48-49]. In the presence of Mo, the intensity of RuO_2 reduction peak decreases strongly and its reduction occurs at higher temperature suggesting an interaction between ruthenium and molybdenum. Furthermore, for the $Ru_{0.1}Mo_{0.9}S_2$/SBA-15 catalyst, this peak does not appear suggesting the absence of separate RuO_2 phase. Going from $Ru_{0.6}Mo_{0.4}$/SBA-15 to $Ru_{0.4}Mo_{0.6}$/SBA-15 catalysts the peak belonging to RuO_2 reduction is shifted towards higher temperatures (from 246 ºC to 288 ºC, respectively). This is probably because the polarization of Ru-O bonds by Mo ions making them more ionic and consequently more difficult to reduce.

The TPR profile of Mo/SBA-15 catalyst exhibits two reduction peaks at about 521 ºC and 700 ºC (Figure 4(a)). The first reduction peak is associated whit the reduction of $MoO_3 \rightarrow MoO_2$, while the higher reduction temperature is characteristic to $MoO_2 \rightarrow Mo^0$ reduction of polymeric octahedral molybdenum species [50-52]. For Ru-containing catalysts, the latter process is less important. After ruthenium incorporation into Mo/SBA-15, the intensity of the peak associated with the reduction $Mo^{4+} \rightarrow Mo^0$ decreases and the corresponding hydrogen consumption occurs at lower temperature. Noticeably, for the $Ru_{0.6}Mo_{0.4}$/SBA-15, the reduction temperature of Mo^{4+} species diminished drastically from 700 °C to 600 °C. For the $Ru_{0.6}Mo_{0.4}$/SBA-15 sample, the $Mo^{4+} \rightarrow Mo^0$ transformation appears as a shoulder of the most intense peak indicative of reduction of MoO_3 species. The effect of ruthenium ions on the reducibility of Mo^{6+} species is no linear with Ru content. The lower reduction temperature for the Mo^{6+} species is observed for the $Ru_{0.4}Mo_{0.6}S_2$/SBA-15 catalyst (494 °C) followed by $Ru_{0.2}Mo_{0.8}$/SBA-15 (506 °C) and $Ru_{0.6}Mo_{0.4}$/SBA-15 (510 °C). The shift to lower reduction temperature strongly suggests the interaction between ruthenium and molybdenum species. Thus, TPR data indicate that a synergy effect between Ru and Mo might occur which could be reflected in the performance of these catalysts.

3.3. Characterizations of the Sulfided Catalysts.

3.3.1. Textural Properties.

The textural properties of the freshly sulfided $Ru_xMo_{(1-x)}S_2$/SBA-15 catalysts were studied by N_2 adsorption-desorption isotherms at -196 ºC (Figure 5). According to the IUPAC classification [53], the N_2 adsorption-desorption isotherms of all catalysts display type II isotherm with appreciable hysteresis loops of type H3. Usually, three well-defined stages can be identified, (i) a slow increase in nitrogen uptake at low relative pressures,

corresponding to monolayer–multilayer adsorption on the pore walls, (ii) a sharp step at intermediate relative pressures indicative of capillary condensation in mesopores, and (iii) a plateau at high relative pressures associated with multilayer adsorption on the external surface. The Mo-containing catalysts show two well defined capillary condensation steps, in comparison whit the monometallic RuS_2/SBA-15 catalyst, which showed a single stage capillary condensation. The first hysteresis loop for these catalysts starts at partial pressure of about 0.22–0.65, indicating the presence of framework mesoporosity. The second hysteresis loop starting at partial pressure of about 0.70-0.55 is due to textural inter-particle mesoporosity or macroporosity. On the other hand, the mono capillary condensation observed in the monometallic RuS_2/SBA-15 catalyst clearly indicates this sample exhibits, in addition to the framework-confined porosity (structural porosity), a uniform textural porosity.

The pore structure parameters, such as specific area (S_{BET}), cumulative pore volume (V_p), pore diameter (d_p) and NS_{BET} values are listed in Table 3. The pure SBA-15 support manifests the highest specific area 894 m^2g^{-1}. As expected, the S_{BET} specific area value decreases with Mo and Ru loading on the support. The values of S_{BET} of SBA-15-supported samples follow the order: $Ru_{0.4}Mo_{0.6}S_2 > Ru_{0.2}Mo_{0.8}S_2 > Ru_{0.6}Mo_{0.4}S_2 > Ru_{0.1}Mo_{0.9}S_2 > RuS_2 > MoS_2$. On the basis of this trend, one can conclude that S_{BET} values decrease not linearly in the region of medium Mo concentrations however the decrease of surface area is less pronounced that at high or low Mo-concentrations. The monometallic MoS_2/SBA-15 catalyst shows the largest drop in surface area among the catalysts studied. The pore diameter and pore volume slightly decreases with the loading of Mo-Ru phases (Table 3). Comparing textural parameters of the naked SBA-15 substrate with that on metal loaded systems, the pore diameter values decrease between 5 to 12%, and a little more between 16 to 21% for the pore volume values. The higher drop in both V_p and d_p values was observed for the monometallic MoS_2/SBA-15 catalyst while the lowest drop was observed for the bimetallic $Ru_{0.4}Mo_{0.6}S_2$/SBA-15 and $Ru_{0.2}Mo_{0.8}S_2$/SBA-15 catalysts.

In order to follow the Ru-induced changes in the localization of the Mo species in the support structure, the normalized S_{BET} values were calculated using the following equation [54]:

$$NS_{BET} = (S_{BET \ of \ catalyst})/[(1-y) \ x \ S_{BET \ of \ support}]$$

where NS_{BET} is normalized S_{BET} and y is the weight fraction of the supported phases. As seen in Table 3, all samples displayed NS_{BET} values in range 0.82-0.93 indicating that the Ru and Mo species can be mainly located in the inner catalyst structure [54]. Noticeably, the $Ru_{0.4}Mo_{0.6}S_2$/SBA-15 catalyst exhibited the most homogeneous metal oxide dispersion among the catalysts studied, as deduced from its highest NS_{BET} value very close to 1 (0.93).

3.3.2. X-Ray Diffraction (XRD).

The X-ray diffraction patters of the freshly sulfided $Ru_xMo_{(1-x)}S_2$/SBA-15 catalysts in the 2θ interval from $10°$ to $80°$ are shown in Figure 6. The X-ray patterns of the samples show a broad line between 15 and 30 °, originated from the amorphous part of the silica support. No reflections belonging to crystalline molybdenum phases were observed. The higher-loaded Ru catalysts (RuS_2/SBA-15 and $Ru_{0.6}Mo_{0.4}S_2$/SBA-15) exhibited peaks reflections characteristics to the RuS_2 phase. The monometallic Ru catalyst (RuS_2/SBA-15) shows two reflection peaks at 27.4 ° and 54.0 ° in 2θ, which are associated with the (111) and (113) planes, respectively, of cubic RuS_2 crystalline (JCPDS 00-012-0737) [55]. The diffraction peak significantly decreases when molybdenum is incorporated ($Ru_{0.6}Mo_{0.4}S_2$/SBA-15 catalyst), besides the diffraction at 54.0 ° in 2θ was not observed. These diffraction peaks disappeared in the catalysts with higher Mo contents. One can conclude that the presence of molybdenum species results in the formation of highly dispersed sulfided phases.

3.3.3. X-ray Photoelectron Spectroscopy (XPS).

Information about the metal surface exposure and the type of species formed in the freshly sulfided catalysts were obtained from X-ray photoelectron spectroscopy. The Mo 3d and Ru 3p core-level spectra of the freshly sulfide $Ru_xMo_{(x-1)}S_2$/SBA-15 catalysts are shown in Figures 7 and 8, respectively. The binding energies (BE) values of the Mo $3d_{5/2}$, Ru $3p_{3/2}$, S 2p core levels and $\Delta Mo(Ru)$ separation energies are shows in Table 4. All catalysts have the S $2p_{3/2}$ peak at 161.2 ± 0.1 eV, which is characteristic of S^{2-} ions [42, 56]. The absence of a second component of BE around 168 eV, where sulfate species are usually observed, indicates that the experimental procedure followed during sulfidation and sample transfer within the spectrometer chamber was efficient in avoiding air contact [54]. The Mo 3d spectra of all catalysts showed the BE of the most intense Mo $3d_{5/2}$ peak at 228.5 ± 0.4 eV. This value is somewhat higher than that usually observed at 228 eV for stoichiometric MoS_2 [57]. This is likely due to the interaction of molybdenum species with the support surface, then the electrons of the molybdenum environment are slightly attracted by the support, which leads to a slight increase of BE values. The absence of peaks corresponding to oxy-sulfide species (like $MoO_2S_2^{2-}$) indicates that Mo sulfidation is complete. Nonetheless, one can see important changes in the BE values of Mo 3d core level upon Ru ions loading. Incorporation of Ru ions decreases the BE values of Mo $3d_{5/2}$ peak. For the low and high Ru containing catalysts (x = 0.1 and 0.6), the BE value of Mo$3d_{5/2}$ level slightly diminished to 228.8 eV, which is very close to the monometallic MoS_2/SBA-15 catalyst. The largest decrease of the BE value was observed for the bimetallic $Ru_{0.4}Mo_{0.6}S_2$/SBA-15 catalyst (from 228.9 to 228.2 eV) followed by the $Ru_{0.2}Mo_{0.8}S_2$/SBA-15 one (from 228.9 to 228.6 eV). The decrease in the BE values indicates that there is an enrichment of electrons in the close vicinity of molybdenum ions, thus increasing the metallic character, such as indicated by DFT calculations.

It is emphasized that we recorded here the Ru 3p core-level spectra because the strong overlapping of C 1s and Ru 3d signals. The Ru 3p spectra of all catalysts showed a single doublet whose most intense $Ru3p_{3/2}$ component of the doublet appeared at a BE of 461.1 ± 0.3 eV. This value is characteristic to the presence of RuS_2 phase [15]. Similarly, changes in the BE values of Ru 3p were observed. With the exception of lower Ru containing catalyst ($Ru_{0.1}Mo_{0.9}S_2$/SBA-15), the presence of Mo ions induces a slight increment of the BE values of Ru $3p_{3/2}$ peak. The higher increase of the BE value was observed in $Ru_{0.4}Mo_{0.6}S_2$/SBA-15 catalyst (0.4 eV), while the BE values of $Ru_{0.2}Mo_{0.8}S_2$/SBA-15 and $Ru_{0.6}Mo_{0.4}S_2$/SBA-15 ones Increased only 0.2 and 0.1 eV, respectively. The drop in the BE observed in Ru 3p signal is related whit the electron enrichment around Ru ion environment, as it was also confirmed by DFT calculations.

The surface Mo/Si, Ru/Si and S/(Mo + Ru) atomic ratios are shows in Table 5. The dispersion of Mo species gradually decreased with the drop of Mo loading, while the dispersion of sulfide Ru species did not decrease linearly with the drop of Ru loading (Table 5). Considering the relative amounts of surface Mo and Ru species, the total dispersion of both sulfide Ru y Mo species on the surface follows the order: $Ru_{0.4}Mo_{0.6}S_2$/SBA-15 > $Ru_{0.2}Mo_{0.8}S_2$/SBA-15 > $Ru_{0.1}Mo_{0.9}S_2$/SBA-15 > $Ru_{0.6}Mo_{0.4}S_2$/SBA-15 > MoS_2/SBA-15 > RuS_2/SBA-15. One can assume that the Ru incorporation has an important effect on the dispersion of the both Mo and Ru sulfide phases, the higher enrichment of the exposure Ru and Mo species was observed on $Ru_{0.4}Mo_{0.6}S_2$/SBA-15 catalyst, while the lowest amount of active species was observed on the respective monometallic catalysts.

The comparison of S/(Mo + Ru) atomic ratio compiled in Table 5, which were calculated taking into account total exposure sulfide Mo and Ru ions, might give an idea about the sulfidation degree of the catalysts. The higher value of the S/(Mo + Ru) at ratio was observed in $Ru_{0.2}Mo_{0.8}S_2$/SBA-15 and $Ru_{0.4}Mo_{0.6}S_2$/SBA-15 catalysts, again was observed in monometallic catalysts, which could indicate that these monometallic samples are less sulfided in comparison with the bimetallic ones.

3.3.4. DRIFTS of Adsorbed Pyridine.

The acidity of sulfided catalysts was evaluated by DRIFT spectra of adsorbed pyridine. Figure 9 shows the DRIFT spectra of adsorbed pyridine in the range of 1400–1700 cm^{-1}. As seen in this figure, all sulfided $Ru_xMo_{(1-x)}S_2$/SBA-15 catalysts exhibit bands at 1638, 1595 (1604 cm^{-1} for RuS_2/SBA-15), 1541, 1486 and 1443 cm^{-1}. The bands at about 1541 and 1638 cm^{-1} are due to pyridinium ions adsorbed on the Brønsted acid sites (PyH$^+$) [58] whereas two bands observed at about 1443 and 1595 cm^{-1} (1604 cm^{-1} for RuS_2/SBA-15) are assigned to pyridine coordinated to Lewis acid sites (PyL) [59]. The band at about 1486 cm^{-1} is the superposition of signals of Lewis and Brønsted acid sites. Since the naked SBA-15 substrate does not display Brønsted acidity [22], we assume that Brønsted acid sites are protons of -SH groups formed during sulfidation. As seen in Fig. 9, the intensity of

the band at 1541 cm^{-1} (Brønsted acidity) follows the trend: Ru$_{0.4}$Mo$_{0.6}$S$_2$/SBA-15 > Ru$_{0.2}$Mo$_{0.8}$S$_2$/SBA-15 > MoS$_2$/SBA-15 >> Ru$_{0.6}$Mo$_{0.4}$S$_2$/SBA-15 ≈ RuS$_2$/SBA-15 (none). The information that Ru$_{0.4}$Mo$_{0.6}$S$_2$/SBA-15 catalyst exhibit largest Brønsted acidity among the catalysts studied is relevant for hydrogen activation during HDS of DBT reaction.

The influence of Ru on the concentration of the Brønsted (B) acid and Lewis (L) acid sites of Ru$_x$Mo$_{(1-x)}$S$_2$/SBA-15 catalysts have been estimated considering areas of bands at 1541 cm^{-1} and 1443 cm^{-1}, respectively. Taking into account the different molar absorption coefficients of protonated and coordinated pyridine [43], additional information has been obtained by comparison of the B/L acidities ratio of the sulfided catalysts given in Table 3. The comparison of B/L ratio for bimetallic catalysts evidences the following trend: Ru$_{0.4}$Mo$_{0.6}$S$_2$/SBA-15 >> MoS$_2$/SBA-15 ≈ Ru$_{0.2}$Mo$_{0.8}$S$_2$/SBA-15 >> Ru$_{0.6}$Mo$_{0.4}$S$_2$/SBA-15 > RuS$_2$/SBA-15. Thus, the Ru$_{0.4}$Mo$_{0.6}$S$_2$/SBA-15 catalyst is unique sample showing a larger B/L ratio then monometallic MoS$_2$/SBA-15. This information is relevant for heterolytic dissociation of hydrogen

3.4. Activity test.

The catalysts were tested in HDS of DBT reaction carried out in a batch reactor at 320 ºC and total hydrogen pressure of 5.5 MPa. The laboratory-synthetized CoMoS/γ-Al$_2$O$_3$ catalyst tested upon the same reaction conditions was used as reference. The comparison of the initial reaction rates of the catalysts is shown in Figure 9. Activity obtained for the MoS$_2$/SBA-15 catalyst was found the lowest among the catalyst series. For the RuS$_2$/SBA-15 catalyst, the reaction rate was almost 2.5 fold the activity of the MoS$_2$/SBA-15 one. This result was expected since early reports about the periodic trends exhibited that Ru provides more activity that Mo [4,28]. As compared with monometallic catalysts, a large activity enhancement was observed for the binary Ru$_x$Mo$_{(1-x)}$S$_2$/SBA-15 systems. Since the activities of all bimetallic systems were greater than the sum of the activities of RuS$_2$/SBA-15 and MoS$_2$/SBA-15 catalysts, a synergetic effect between Ru and Mo occurs. At concentration of x = 0.1 in the Ru$_{0.1}$Mo$_{0.9}$S$_2$/SBA-15 catalyst provides almost twice the activity of RuS$_2$/SBA-15 and 5 times more than that of MoS$_2$/SBA-15. For the Ru concentration (x) of 0.2 and 0.4, it is observed an increase in the catalytic activity of about 50% and 100% more than that obtained for x = 0.1. A further increase led to a drastic decrease in activity. Therefore, the sulfided Ru$_{0.4}$Mo$_{0.6}$S$_2$/SBA-15 catalyst exhibit the best catalyst response in HDS of DBT upon reaction conditions studied. Contrary to this work, the absence of synergy between Ru and Mo was reported for alumina-supported Ru-Mo/γ-Al$_2$O$_3$ catalysts, which were calcined before sulfidation [15]. In comparison to Ru$_{0.4}$Mo$_{0.6}$S$_2$/SBA-15 catalyst, the laboratory-synthetized CoMoS/γ-Al$_2$O$_3$ catalyst exhibited a little larger initial activity (78 vs. 70 x 10^{-8} mol$_{DBT}$ ·g^{-1}·s^{-1}).

Figure 10 shows the the yields of products and HYD/DDS selectivities ratios calculated at 26% of DBT conversion. The reaction products were: biphenyl (BP),

cyclohexylbenzene (CHB) and dicyclohexyl (DCH). It is noted that tetrahydrodibenzothiophene (THDBT) was not detected in the chromatograms. Regardless of the Ru-loading, the main product was biphenyl followed by cyclohexylbenzene. As seen in Scheme 1, BP and CHB were formed *via* direct desulfurization (DDS) and hydrogenation (HYD) reaction routes of DBT transformation, respectively. The monometallic RuS_2/SBA-15 and MoS_2/SBA-15 catalysts did not show the DCH product suggesting their lower HYD function with respect to $Ru_xMo_{(1-x)}S_2$/SBA-15 systems.

When we look at the effect of Ru incorporation into MoS_2 crystal structure on the HYD/DDS selectivity ratios (Fig. 11) we see that for all catalysts this ratio is in the range 0.07-0.43. This clearly indicates the C-S bond cleavage (DDS route) of DBT HDS reaction (DDS) is dominant over the hydrogenation of the aromatics ring (HYD rute). The HYD/DDS selectivity ratio follows the trend: $Ru_{0.4}Mo_{0.6}S_2$/SBA-15 > $Ru_{0.2}Mo_{0.8}S_2$/SBA-15 > $Ru_{0.6}Mo_{0.4}S_2$/SBA-15 > $Ru_{0.1}Mo_{0.9}S_2$/SBA-15 > CoMo(S)/Al_2O_3 > RuS_2/SBA-15 >> MoS_2/SBA-15. The HYD/DDS ratio of the most active $Ru_{0.4}Mo_{0.6}S_2$/SBA-15 catalyst is six-times higher than that achieved on the MoS_2/SBA-15 counterpart. Noticeably, $Ru_{0.4}Mo_{0.6}S_2$/SBA-15 catalyst catalyst showed two-fold higher hydrogenation properties than synthetized CoMoS/γ-Al_2O_3 reference catalyst. For all catalysts, the HYD pathway follows a similar trend as that observed for the catalytic performance (Figure 11); even when the activity falls down to 40%; for $Ru_{0.4}Mo_{0.6}S_2$/SBA-15 to $Ru_{0.6}Mo_{0.4}S_2$/SBA-15 selectivity only changed 25%. The enhancement of HYD/DDS selectivity ratio after Ru incorporation into the base MoS_2/SBA-15 occurs, which is in good agreement with those observed for alumina-supported Ru-Mo catalysts [15].

Considering the DBT HDS reaction mechanism, it is generally assumed that the sulfur vacancies are responsible for the direct sulfur abstraction from DBT (DDS route) whereas the acidic SH groups are involved on the HYD reaction (Scheme 1). Assuming that sulfur vacancies located on both rim and edge sites of MoS_2 phase are responsible for C-S bond hydrogenolysis whereas DBT transformation *via* hydrogenation reaction route occurs exclusively on the rim sites [60], the largest HYD activity of $Ru_{0.4}Mo_{0.6}S_2$/SBA-15 can be due to its largest amount of the rim sites. The enhancement of HYD selectivity observed for this most active catalyst can be explained also considering that the self-produced H_2S might to alter the balance between DDS and HYD active sites inhibiting the DDS route much stronger than the HYD reaction pathway [61]. This is because of the strong competition of the H_2S with DBT for adsorption on vacant sites leading to inhibition of DDS route [61]. However further experiments are needed to confirm this supposition.

3.5. Catalyst activity-structure correlations.

In this work, the combined information obtained from theoretical and experimental catalyst characterization strongly suggests a synergetic effect between ruthenium and molybdenum species. However, a linear dependency of catalytic activity on Ru content (*x*)

in the $Ru_xMo_{(1-x)}S_2$ solid solution was not observed indicating that molybdenum replacement by Ru should be optimized. In fact, the largest synergetic effect was archived for the catalyst prepared with stoichiometry $Ru_{0.4}Mo_{0.6}S_2$. Taking into account the TPR characterization of the oxide precursors, this catalyst exhibits a lowest metal-support interaction with SBA-15 support. After sulfidation, the $Ru_{0.4}Mo_{0.6}S_2$/SBA-15 catalyst demonstrated to be bifunctional in the HDS of DBT reaction through its both metal and acid functions. This can be explained considering that this catalyst exhibited the best metal sulfides dispersion (from XRD), largest specific BET surface area (Table 3), highest Brønsted-to-Lewis acidities ratio (DRIFTS of pyridine) and the largest metal sulfide surface exposure among the catalysts studied (from XPS). Considering the latter factor, it was found a linear correlation between the surface exposure of the Ru and Mo sulfide species and the catalytic performance of the catalysts confirming the importance of the metal sulfide surface exposure on the catalyst activity (Figure 12). In addition, XPS results confirmed total sulfidation of Ru and Mo phases after catalyst activation by sulfidation at 400 ºC (Table 4). This is important observation because much higher sulfidation temperature is needed for the formation of RuS_2 phase with pyrite-like structure on the surface of alumina-supported systems (400 ºC vs. 500 ºC) [62]. The easier sulfidation of the Ru-containing catalysts can be explained considering the formation of well-dispersed crystals of $Ru_xMo_{(1-x)}S_2$ species on the surface of SBA-15 carrier, as deduced from XRD. Finally, considering the catalyst acidic function, a lineal correlation between Brønsted-to-Lewis acidity ratio and initial activity of the catalysts was observed (Fig. 13).

The catalyst activity test shows that HYD/DDS ratio increases with an increase of isomorphic substitution of molybdenum by ruthenium atoms. Particularly, it presents the best hydrogenation behavior for the catalyst with $x = 0.4$ value. It is known that any variation in the selectivity could be due to the capacity of the catalyst for the H_2 activation or to some acid-base sites which could be involved in the hydrogenation step. Indeed, in this work the catalyst with largest HYD function exhibit also the largest acidity confirming that the acidic SH groups are involved in the HYD reaction route. Additional acidity can be formed during HDS od DBT reaction by heterolytic hydrogen dissociation on MoS_2 [63] and RuS_2 [64] leading to the formation of a metal hydride and –SH groups. The catalytic centers for this dissociation are composed of a sulfur vacancy located on a Mo/Ru atom and of a neighbourning sulfur anion; the H-atom having a hydride character is adsorbed on the metal ion whereas the H-atom with protonic character is adsorbed on the sulfur anion forming SH groups [65]. Contrary to Ru-based catalysts, the DFT calculation by Travert et al. [67] suggest hydride bond to Mo are highly unstable. Thus, one might to suppose that the best catalytic behavior of the $Ru_{0.4}Mo_{0.6}S_2$/SBA-15 catalyst can be due to formation of specific centers for heterolytic dissociation of H_2 on the surface of $Ru_{0.4}Mo_{0.6}S_2$ solid solution. However further experiments are needed to confirm this supposition.

Considering the electronic effect, the presence of Ru ions strongly improved the metallic character of the molybdenum species, as confirmed by DFT results. In this sense,

15

the most active $Ru_{0.4}Mo_{0.6}S_2$/SBA-15 catalyst displayed the highest metallic character among the catalysts studied. Considering the theoretical results shown in Figures 3(a)-(c), an increase in the catalyst hydrogenation function is closely correlated with the gain in the density of states of the samples. Although it is true that in the present study the 4d orbitals play an important role in optimizing catalytic activity, which is in agreement with Chianelli [28], the present results show that the enrichment with Ru also promotes the participation of the 3p sulfur orbitals (Figure 3(a)). This is evident when the respective orbital contributions of MoS_2 and RuS_2 monometallics are compared. On the other hand, the presence of Ru in the $Ru_xMo_{(1-x)}S_2$/SBA-15 catalysts promotes the amphotericism and favors the volcano-curve activity trend with maximum of activity observed for catalyst having Ru content around x = 0.44. This suggest the enhancement of the charge transference processes due to the presence of ruthenium, which is reflected in a high metallic character of the $Ru_xMo_{(1-x)}S_2$/SBA-15 catalysts having theoretical Ru content of 0.44. In agreement with both experimental and theoretical results, one can conclude that the electron receptors are the molybdenum ions, while the ruthenium ions localized in the electronic environmental of molybdenum ions increased the metallic character of Mo ions.

Summarizing, from the activity results, it is concluded that only the formation of $Ru_xMo_{(1-1)}S_2$ solid solution is relevant for the catalyst activity, but not the amount of Ru incorporated in this solution. The superior activity of sulfided $Ru_{0.4}Mo_{0.6}S_2$/SBA-5 catalyst in the HDS of DBT reaction is linked with its best physicochemical properties and the Ru-induced metallic character of MoS_2 phase, as demonstrated by DFT calculations. The theoretical results are in good agreement with those reported for the catalysts having the so-called "*brim sites*" having metallic character [68-69]. Thus, an increase of HYD/DDS selectivity ratio with an increase of Ru loading might to suggest the presence of $Ru_xMo_{(1-x)}S_2$ solid solution having a large amount of "*brim sites*". However, this should be a subject of future research.

4. Conclusions.

This work clearly demonstrated that the formation of $Ru_xMo_{(1-x)}S_2$ solid solution enhanced the catalytic behavior of the $Ru_xMo_{(1-x)}S_2$/SBA-15 systems through electronic, synergetic and structural effects. Through the density functional theory method (DFT), we have investigated the electronic properties of a set of crystalline structures which belongs to the $Ru_xMo_{(1-x)}S_2$/SBA-15 catalysts. Most of those structures were obtained by introducing impurities in the MoS_2 crystalline structure. Results show that the enrichment with Ru, promotes a greater electronic participation (DOS at the Fermi level) of the different atoms in the $Ru_xMo_{(1-x)}S_2$/SBA-15 catalysts, which for the theoretical concentrations considered in our calculations, presents the highest value at x = 0.44. The increase of the catalyst HYD function shows a behavior well correlated with the increases in DOS previously mentioned. On the contrary to the HYD rute, it was found that the increase in the catalysis by the

hydrodesulfurization reaction path, is closely related with a higher participation at the Fermi level of sulfur atoms. Supported on the Mulliken charges analysis, it is observed that an amphoteric behavior for all atomic species is desirable to reach an ideal electronic behavior, under which the HYD catalysis achieves the best performance. According to both theoretical/experimental results, these suggest that the concentration value should be found around $x = 0.44$.

Acknowledgments.

References.
[1]   N. Siddiqui, S. Tauseef and K. Bansal, Advances in Health and Environment Safety, 1st ed. (Springer Singapore, 2018).

[2]   D. Y. C. Leung, G. Caramanna and M. M. Maroto-Valer, Renew. Sust. Energ. Rev. 39, 426 (2014).

[3]   S. F. Tie and C. W. Tan, Renew. Sust. Energ. Rev. 20, 82 (2013).

[4]   T.A. Pecoraro and R. R. Chianelli, J. Catal. 67, 430 (1981).

[5]   S. Harris and R. Chianelli, J. Catal. 86, 400 (1984).

[6]   T. G. Harvey and T. W. Matheson, J. Catal. 101, 253 (1986).

[7]   M. Wojciechowska, M. Pietrowski, B. Czajka and S. Łomnicki, Cat. Lett. 87, 3 (2003).

[8]   T. C. Ho, Cat. Lett. 89, 21 (2003).

[9]   J.A. De los Reyes, Appl. Catal. A: Gen. 322, 106 (2007).

[10] M. Cattenot, C. Geantet, C. Glasson and M. Breysse, Appl. Catal. A: Gen. 213, 217 (2001).

[11] R.M. Navarro, P. Castaño, M.C. Álvarez-Galván and B. Pawelec, Catal. Today 143, 108 (2009).

[12] B. Pawelec, R.M. Navarro, P. Castaño, M.C. Álvarez-Galván, J.L.G. Fierro, Energy & Fuels 23, 1364 (2009).

[13] T. Isoda, S. Nagao, X. Ma, Y. Korai and I. Mochida, Energy & Fuels 10, 482 (1996).

[14] Y. Muhammad, Y. Lu, C. Shen and C. Li, Energy Conversion and Management, 52, 1364-1370 (2011).

[15] P.C.H. Mitchell, C.E. Scott, J.-P. Bonnelle and J.G. Grimblot, J. Catal. 107, 482 (1987).

[16] J. Shabtai, Q. Guohe, K. Balusami, N.K. Nag and F.E. Massoth, J. Catal., 113, 206 (1988).

[17] C. Geantet, S. Gobolos, J.A. de los Reyes, M. Cattenot, M. Vrinat and M. Breysse, Catal. Today, 10, 665 (1991).

[18] Z. Vít, D. Gulková, L. Kaluža and M. Zdražil, J. Catal., 232, 447 (2005).

[19] M. Breysse, R. Frety and B. Benaichouba, P. Bussire, Radiochem. Radioanal. Lett., B59, 265 (1983).

[20] P. Afanasiev and I. Bezverkhyy, Appl. Catal. A: Gen. 322, 129 (2007).

[21] R. Huirache Acuña, R. Nava, C.L. Peza-Ledesma, J. Lara-Romero, G. Alonso-Núñez, B. Pawelec and E.M. Rivera-Muñoz, Materials, 6(9), 4139 (2013).

[22] F. Zhang, Y. Yan, H. Yang, Y. Meng, C. Yu, Bo Tu and D. Zhao, J. Phys. Chem. B. 109 8723 (2005).

[23] M. Breysse, P. Afanasiev, C. Geantet and M. Vrinat, Catal. Today. 86, 5-16 (2003)

[24] A. Romero-Pérez, A. Infantes-Molina, E. Rodríguez-Castellón and A. Jiménez-López, Appl. Catal. B: Environ. 97, 257 (2010).

[25] A. Infantes-Molina, A. Romero-Pérez, E. Finocchio, G. Busca, A. Jiménez-López and E. Rodríguez-Castellón, J. Catal. 305, 101 (2013).

[26] A. Infantes-Molina, A. Romero-Pérez, V. Sánchez-González, B. Pawelec, J.L.G. Fierro, A. Jiménez-López and E. Rodríguez-Castellón, ACS Catalysis, 1, 175, (2011).

[27] N.L. Torres-García, R. Salas, R. Maya-Yescas and J.M. Rivera-Garnica, Inter. J. Chem. Reactor Engineering, 20170264 (2018).

[28] R. R. Chianelli, Oil & Gas Science and Technology - Rev. IFP 61, 503 (2006).

[29] B. Schönfeld, J. J. Huang and S. C. Moss, Acta Crystallogr. B 39, 404 (1983).

[30] A. Tan and S. Harris, Inorg. Chem. 37, 2215 (1998).

[31] Software from Accelrys Inc.: http://www.accelrys.com.

[32] B. Delley, J. Chem. Phys. 92, 508 (1990).

[33] B. Delley, J. Chem. Phys. 113, 7756 (2000).

[34] J. P. Perdew, K. Burke, and M. Ernzerhof, Phys. Rev. Lett. 77, 3865 (1996).

[35] L. F. Mattheiss, Phys. Rev. B 8, 3719 (1973).

[36] A. J. Grant, T. M. Griffths, G. D. Pitt and A. D. Yoffe, Phys. Rev. B 8, 3719 (1973).

[37] A. Kuc, N. Zibouche and T. Heine, Phys. Rev. B 83, 245213 (2011).

[38] W. S. Yun, S. W. Han, C. S. Hong, I. G. Kim and J. D. Lee, Phys. Rev. B 85, 033305 (2012).

[39] S. Ahmad and S. Mukherjee, Graphene 85, 52 (2014).

[40] D. Zhao, Q. Huo, J. Fend, B.F. Chmelka, G.D. Stucky, J. Am. Chem. Soc. 120 (1998) 6024.

[41] Y. Yue, A. Gedeon, J. Bonardt, J. Espinose, N. Melosh, J. Fraissard, Chem. Commun. 19 1967 (1999).

[42] J.N. Díaz de León, T.A. Zepeda, G. Alonso-Núñez, D.H. Galván, B. Pawelec and S. Fuentes, J. Catal 321, 51 (2015).

[43] M. Guisnet, P. Ayrault, C. Couanceau, M.F. Alvarez and J. Datka, J. Chem. Soc. Faraday Trans. 93, 1661 (1997).

[44] D.D. Whitehurst, T. Isoda and I. Mochida, Adv. Catal. 43, 3450 (1998).

[45] M. Kertesz and R. Hoffmann, J. Am. Chem. Soc. 106, 3453 (1984).

[46] M. C. Zonnevylle and R. Hoffmann, Surf. Science, 199, 320 (1988).

[47] J.A. de los Reyes, Appl. Catal. A: Gen. 322, 106 (2007).

[48] N. Hamzah, N. M. Nordin, A. H. A. Nadzri, Y. A. Nik, M. B. Kassim and M. A. Yarmo, Appl. Catal., A, 419–420, 133 (2012)..

[49] L. Hua, X. Liua, Q. Wangc and Y. Zhou, RSC Adv. 7, 21507 (2017).

[50] P. Arnoldy, J.C.M. de Jong and J.A. Moulijn, J. Phys. Chem., 89, 4517 (1985).

[51] F.B. Noronha, M.A.S. Baldanza and M. Schmal, J. Catal. 188, 270 (1999).

[52] M.C. Abello, M.F. Gomez and O. Ferreti, Appl. Catal. A: Gen. 207, 421 (2001).

[53] M. Thommes, K. Kaneko, A.V. Neimark, J.P. Oliver, F. Rodriguez-Reinoso, J. Rouquerol and K.S.W. Sing, Pure. Appl. Chem. 87(9-10), 1051 (2015).

[54] L. Vradman, M.V. Landau, D. Kantorovich, Y. Koltypin and A. Gedanken, Microp. Mesop. Mat. 70, 307 (2005).

[55] X-ray diffraction NIST Standard Reference Database (https://srdata.nist.gov/gateway/gateway?keyword=x+ray+diffraction)

[56] T.A. Zepeda, B. Pawelec, R. Obeso-Estrella, J.N. Díaz de León, S. Fuentes, G. Alonso-Núñez and J.L.G. Fierro, Appl. Catal. B: Env. 180, 569 (2016).

[58] R.I. Declerck-Grimee, P. Canesson, R.M. Friedman, J.J. Fripiat, J. Phys. Chem. 82(8) (1978) 889.

[59] Parry, E.P., J. Catal., 2 (1963) 371

[60] J.W. Ward. J. Catal. 9 (1967) 225.

[61] M. Daage, R.R. Chianelli and A.F. Ruppert, Stud. Surf. Sci. Catal. 75, 571 (1993).

[62] B.M. Vagelaar, N. Kagami, A.D. van Langeveld, S. Eijsbouts and J.A. Moulijn, Prep. Pap.-Am. Chem. Soc., Div. Fuel Chem. 48(2), 548 (2003).

[63] J. A. De Los Reyes, S. Göbölös, M. Vrinat and M. Breysse, Catal Lett 5, 17-24 (1990).

[64] A.B. Anderson, Z.Y. Al-Saigh and W.K. Hall, J. Phys. Chem. 92, 803 (1988).

[65] F. Frechard and P. Sautet, Surf. Sci. 389, 131 (1997).

[66] G. Pérot, Fuel Chemistry Division Preprints 48(1), 127 (2003).

[67] A. Travert, H. Nakamura, R.A. van Santen, S. Cristol, J.-F. Paul and E. Payen, J. Am. Chem. Soc. 124, 7084 (2002).

[68] H. Topsøe, B. Hinnemann, J.K. Nørskov, J.V. Lauritsen, F. Besenbacher, P.L. Hansen, G. Hytoft, R.G. Egeberg and K.G. Knudsen, Catal Today 107-108, 12-22 (2005).

[69] J.V. Lauritsen, M.V. Bollinger, E. Lægsgaard, K.W. Jacobsen, J.K. Nørskov, B.S. Clausen, H. Topsøe and F. Besenbacher, J Catal. 221, 510-522 (2004).

Table 1. Cell parameters a and c and band gap values computed theoretically and experimentally for the MoS_2 and RuS_2 bulk compounds.

Compound	Theoretical			Experimental		
	a[Å]	c[Å]	Direct Gap [eV]	a[Å]	c[Å]	Direct Gap [eV]
MoS2	3.20	12.60	1.00	3.16[29,30]	12.93[40,41]	1.2[42,45]
RuS2	5.61	5.61	1.36	5.61[32]	5.61[45]	1.3[46]

Table 2. Theoretical metal loadings and chemical composition of the calcined samples (from ICP-AES)

Sample	Theoretical Loading			Experimental Loading		
	Ru %wt.	Mo %wt.	Ru/(Ru+Mo) at	Ru %wt.	Mo %wt.	Ru/(Ru+Mo) at
Mo/SBA-15	0.00	12.09	0	0.00	12.40	0.00
$Ru_{0.1}Mo_{0.9}$/SBA-15	1.28	10.88	0.10	1.39	10.11	0.12
$Ru_{0.2}Mo_{0.8}$/SBA-15	2.56	9.67	0.20	2.21	9.54	0.18
$Ru_{0.4}Mo_{0.6}$/SBA-15	5.13	7.25	0.40	5.90	7.31	0.43
$Ru_{0.6}Mo_{0.4}$/SBA-15	7.69	4.84	0.60	7.33	5.31	0.57
Ru/SBA-15	12.81	0.00	1.00	11.64	0.00	1.00

Table 3. Textural properties[a] of the pure SBA-15 support and sulfided catalysts as determined by N_2 adsorption desorption isotherms[a] at -196 ºC.

Sample	S_{BET} (m^2/g)	dp (nm)	Vp (cm^3/g)	NS_{BET}[b]
SBA-15	894	4.2	1.23	-
MoS_2/SBA-15	641	3.7	0.96	0.82
$Ru_{0.1}Mo_{0.9}S_2$/SBA-15	653	3.8	0.97	0.83
$Ru_{0.2}Mo_{0.8}S_2$/SBA-15	691	4.0	1.03	0.88
$Ru_{0.4}Mo_{0.6}S_2$/SBA-15	718	4.0	1.03	0.93
$Ru_{0.6}Mo_{0.4}S_2$/SBA-15	680	3.9	1.01	0.87
RuS_2/SBA-15	663	3.8	0.97	0.84

[a] S_{BET}: specific surface area; dp: pore diameter; Vp: total pore volume

[b] NS_{BET}: normalized BET surface.

Table 4. Binding energies (eV) of core-electrons of the sulfided $Ru_xMo_{(1-x)}S_2$ catalysts.

Catalyst	Mo $3d_{5/2}$	$\Delta_{Mo(5/2-3/2)}$	Ru $3p_{3/2}$	$\Delta_{Ru(3/2-1/2)}$	S 2p
MoS_2/SBA-15	228.9	3.20	-	-	161.9
$Ru_{0.1}Mo_{0.9}S_2$/SBA-15	228.8	3.19	461.9	22.2	162.0
$Ru_{0.2}Mo_{0.8}S_2$/SBA-15	228.6	3.19	462.1	22.2	161.9
$Ru_{0.4}Mo_{0.6}S_2$/SBA-15	228.2	3.20	462.3	22.2	161.9
$Ru_{0.6}Mo_{0.4}S_2$/SBA-15	228.8	3.19	462.0	22.1	161.9
RuS_2/SBA-15	-	-	461.9	22.2	161.9

Table 5. Surface atomic ratios of the sulfided $Ru_xMo_{(1-x)}S_2$/SBA-15 catalysts

Catalyst	Mo/Si at	Ru/Si at	(Ru-Mo)/Si	S/(Ru+Mo)
MoS_2/SBA-15	0.016	-	0.016	1.28
$Ru_{0.1}Mo_{0.9}S_2$/SBA-15	0.016	0.002	0.018	1.33
$Ru_{0.2}Mo_{0.8}S_2$/SBA-15	0.015	0.004	0.019	1.41
$Ru_{0.4}Mo_{0.6}S_2$/SBA-15	0.014	0.010	0.024	1.41
$Ru_{0.6}Mo_{0.4}S_2$/SBA-15	0.008	0.009	0.017	1.37
RuS_2/SBA-15	-	0.015	0.015	1.22
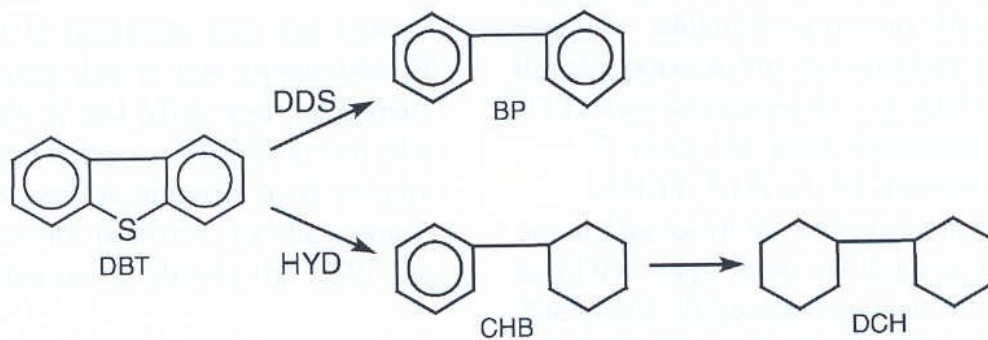
Scheme 1. HDS of DBT reaction scheme for the sulfided NiMoW/HMS and NiMoW/HMS-Ti catalysts, where DDS and HYD are direct desulfurization and hydrogenation reaction pathways, respectively; DBT: dibenzothiophene; CHB: cyclohexylbenzene; BP: biphenyl; DCH: dicyclohexyl.
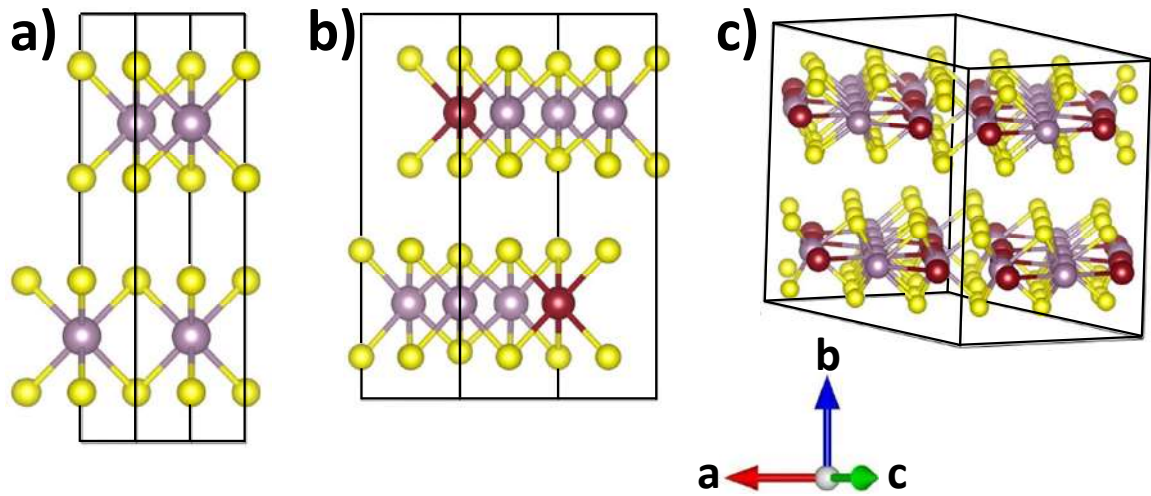
Figure 1. Illustration of the distinct unit cells for some of the crystalline $Ru_xMo_{(1-x)}S_2$ phase considered in the computations: (a) $x = 0$, (b) $x = 0.25$ and (c) $x = 0.44$.
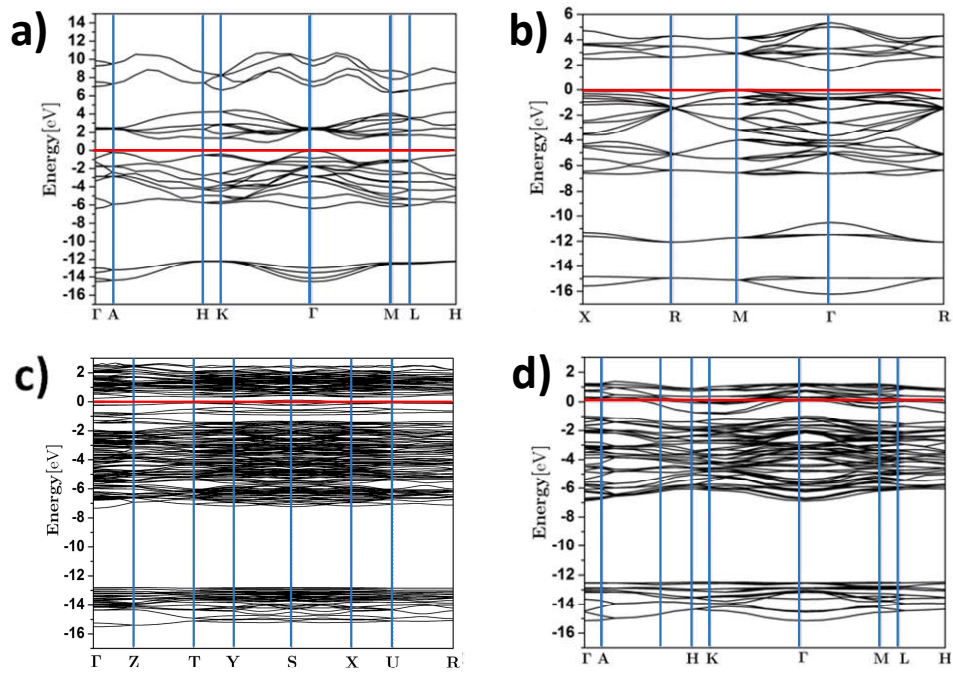

Figure 2. Band structure for the crystalline $Ru_xMo_{(1-x)}S_2$ phase: (a) $x = 0$, (b) $x = 0.25$, (c) $x = 0.44$ and (d) $x = 1$. The horizontal solid red line indicates the Fermi level localized at 0 eV.
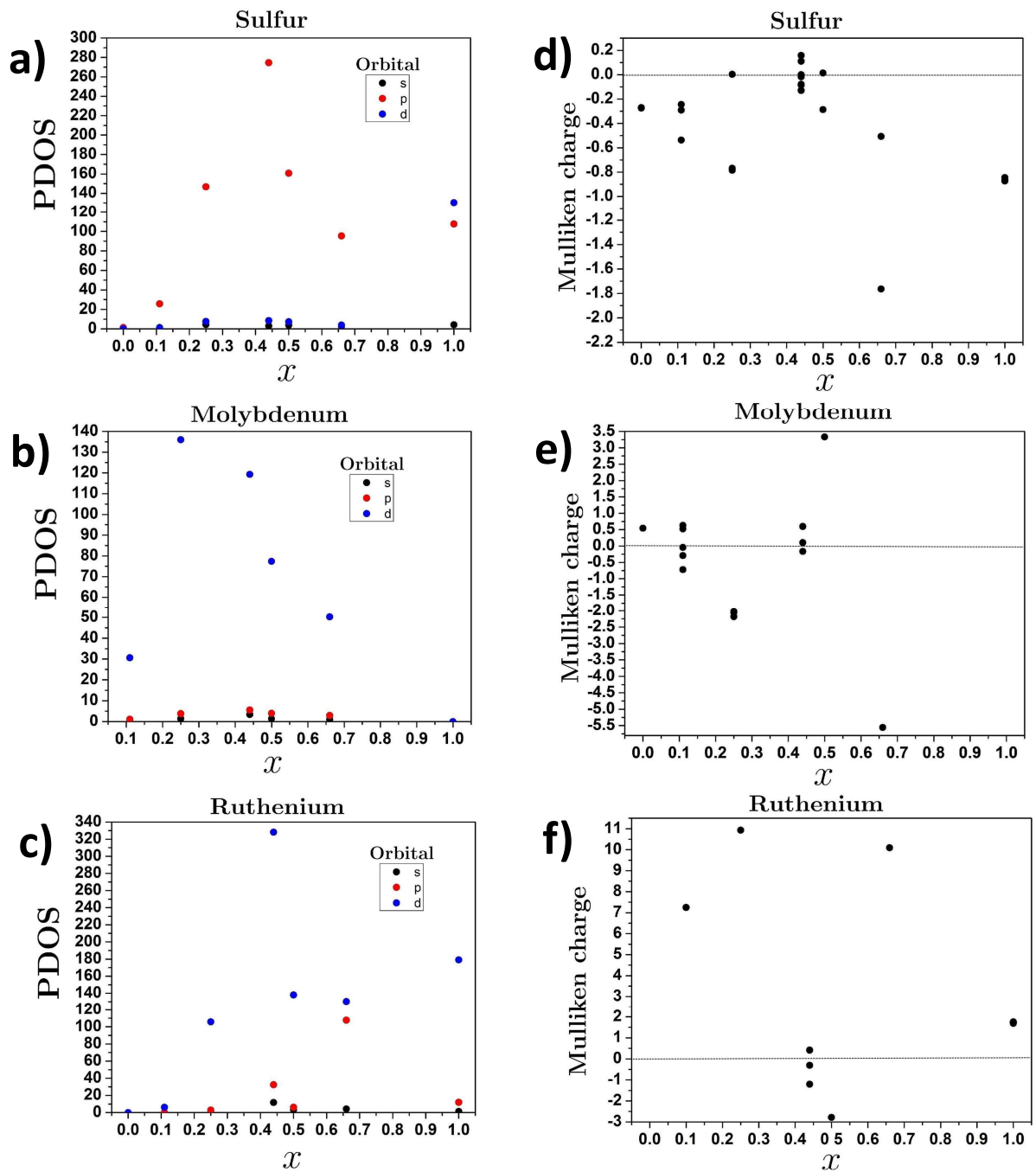
Figure 3. PDOS (a-c) and Mulliken (d-e) charge for the S, Mo and Ru atoms against the Ru concentration x. PDOS values are computed at the Fermi level localized at 0 eV.
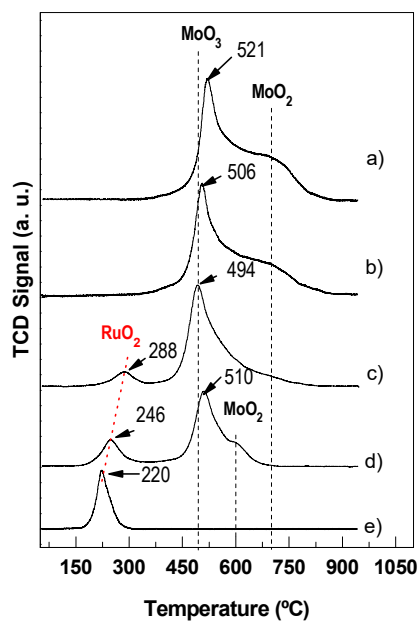
Figure 4. TPR profiles of the calcined $Ru_xMo_{(1-x)}$/SBA-15 catalysts: (a) $x = 0$; (b) $x = 0.2$; (c) $x = 0.4$; (d) $x = 0.6$ and (e) $x = 1$.
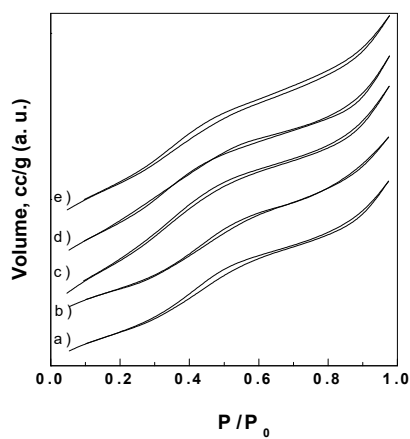
Figure 5. N_2 adsorption-desorption isotherms for the sulfided $Ru_xMo_{(1-x)}S_2$/SBA-15 catalysts: (a) $x = 0$; (b) $x = 0.2$; (c) $x = 0.4$; (d) $x = 0.6$ and (e) $x=1$.
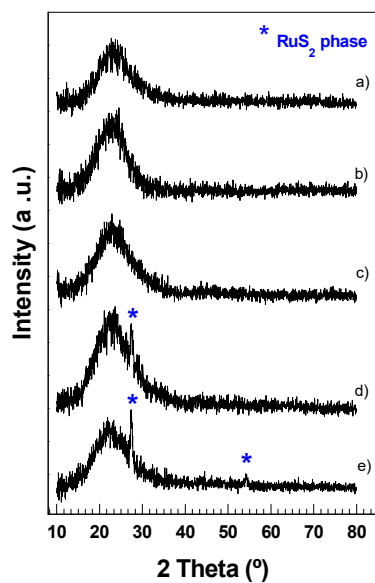
Figure 6. X-ray diffraction patterns of the sulfided $Ru_xMo_{(1-x)}S_2$/SBA-15 catalysts: (a) $x =$ 0; (b) $x = 0.2$; (c) $x = 0.4$; (d) $x = 0.6$ and (e) $x=1$.
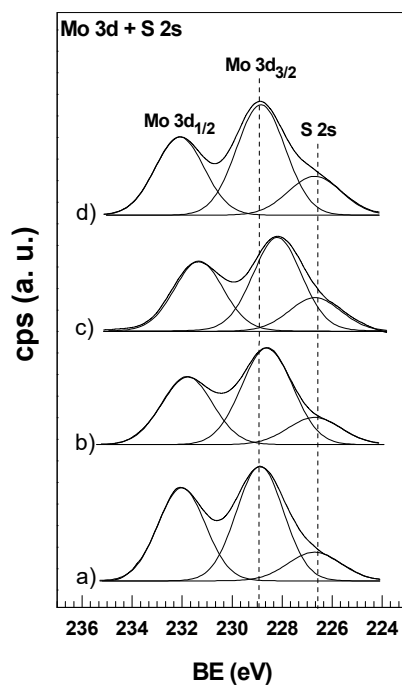
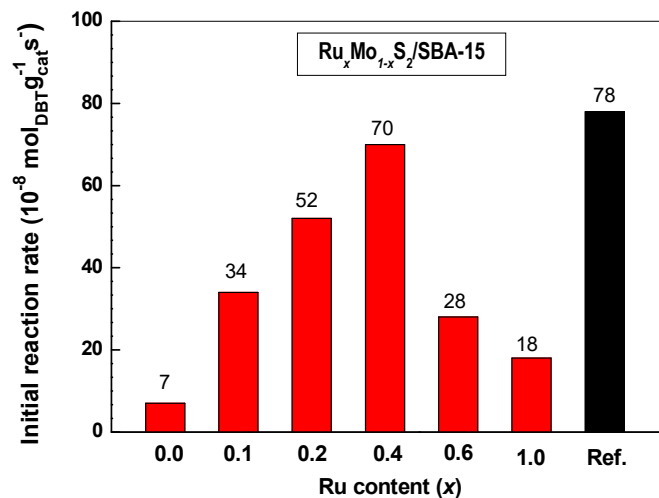**Figure 7**. Mo 3d core level spectra of the sulfided $Ru_xMo_{(1-x)}S_2$/SBA-15 catalysts: (a) $x =$ 0; (b) $x = 0.2$; (c) $x = 0.4$ and (d) $x = 0$.
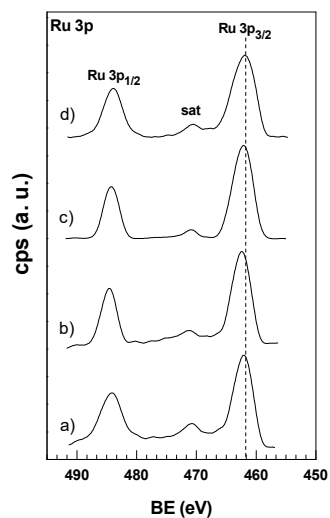
Figure 8. Ru 3p core level spectra of the sulfided $Ru_xMo_{(1-x)}S_2$/SBA-15 catalysts: (a) $x =$ 0; (b) $x = 0.2$; (c) $x = 0.4$; (d) $x = 0.6$ and (e) $x = 1$.
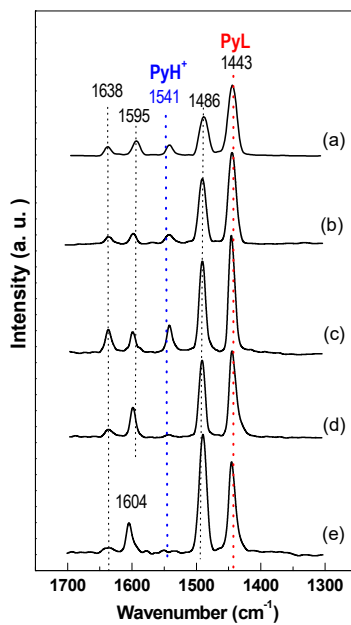
Figure 9. DRIFT spectra of adsorbed pyridine for the sulfided $Ru_xMo_{(1-x)}S_2$/SBA-15 catalysts: (a) $x = 0$; (b) $x = 0.2$; (c) $x = 0.4$; (d) $x = 0.6$ and (e) $x = 1$.

Figure 10. Influence of the Ru content (x) on the initial reaction rate of $Ru_xMo_{(1-x)}S_2$/SBA-15 catalysts in HDS of DBT reaction (batch reactor, T= 320 ºC, total H_2 pressure of 5.5. MPa). The CoMoS/γ-Al_2O_3 catalyst was used as reference.
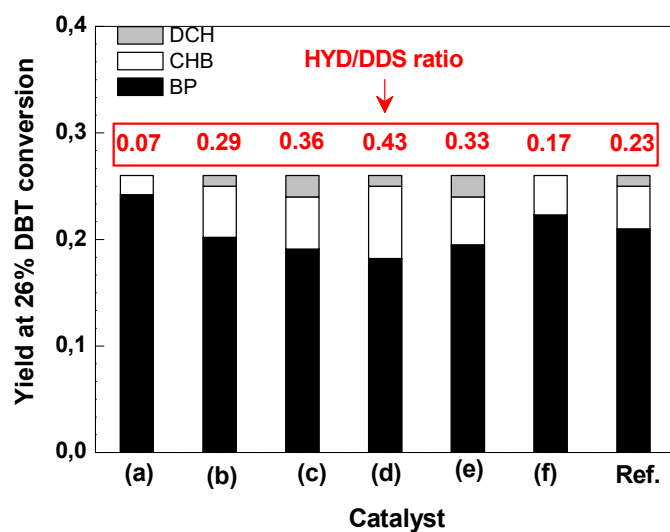
Figure 11. Yields of the products at 26% of DBT conversion and HYD/DDS selectivities ratio in HDS of DBT reaction over $Ru_xMo_{(1-x)}S_2$/SBA-15 catalysts (batch reactor, T= 320 ºC, total H_2 pressure of 5.5. MPa): (a) = MoS_2; (b) = $Ru_{0.1}Mo_{0.9}S_2$; (c) = $Ru_{0.2}Mo_{0.8}S_2$; (d) = $Ru_{0.4}Mo_{0.6}S_2$; (e)= $Ru_{0.6}Mo_{04}S_2$ and (f) = MoS_2. The laboratory-made CoMo/γ-Al_2O_3 sulfide catalyst was used as reference
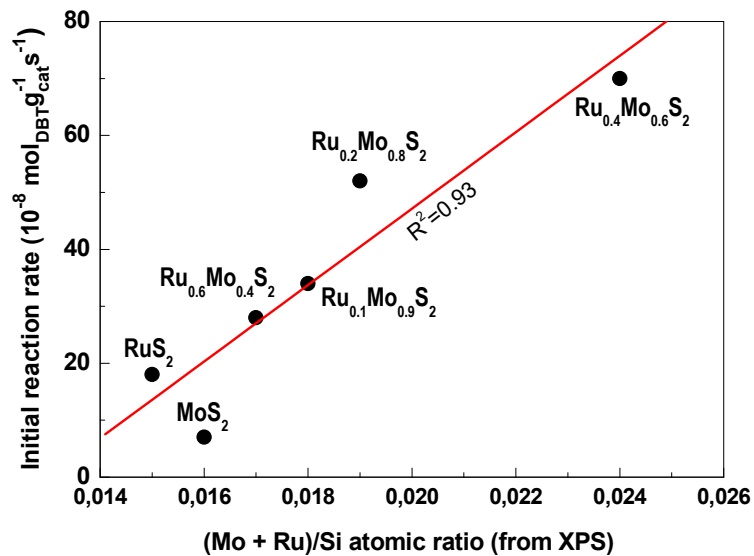
28

Figure 12. Influence of the surface exposure of Mo and Ru sulfide species on the initial reaction rate of HDS of DBT reaction over sulfided $Ru_xMo_{1-x}S_2$/SBA-15 catalysts. The reaction conditions were: batch reactor, T= 320 ºC and total H_2 pressure of 5.5. MPa.
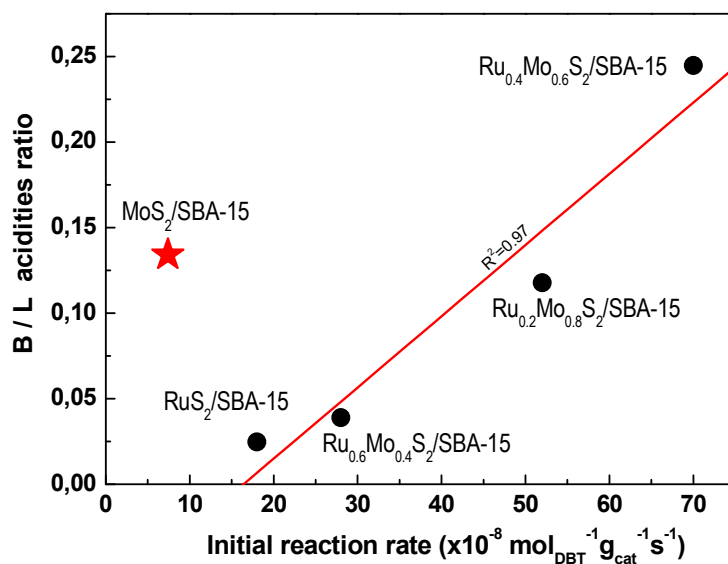

Figure 13. Influence of the B/L acidities ratio of the sulfided $Ru_xMo_{(1-x)}S_2$/SBA-15 catalysts on the initial rate of HDS of DBT reaction